Research Square

Preprints are preliminary reports that have not undergone peer review.
They should not be considered conclusive, used to inform clinical practice,
or referenced by the media as validated information.

Assessment of Published Finite-Fault Models for the 2025 Kamchatka Earthquake by Comparison with Satellite Gravity Observations

Yusaku Tanaka

tanaka-u39@aoni.waseda.jp

Waseda University: Waseda Daigaku https://orcid.org/0000-0001-9305-7150

Research Article

Keywords: 2025 Kamchatka earthquake, GRACE Follow-On, Satellite gravimetry, Coseismic gravity changes, Finite-fault models, Earthquake source model validation

Posted Date: November 26th, 2026

DOI: https://doi.org/10.21203/rs.3.rs-11655298/v1

License: This work is licensed under a Creative Commons Attribution 4.0 International License.
Read Full License

Assessment of Published Finite-Fault Models for the 2025 Kamchatka Earthquake by Comparison with Satellite Gravity Observations

Yusaku TANAKA (corresponding)

Faculty of Education and Integrated Arts and Sciences, Waseda University

(address) 1-6-1 Nishiwaseda, Shinjuku-ku, Tokyo 169-8050, Japan

(E-mail) tanaka-u39@aoni.waseda.jp

Abstract

The 2025 Mw 8.8 Kamchatka earthquake provides an opportunity to evaluate earthquake source models using satellite gravity observations independently of conventional seismic and geodetic measurements. Its location along the Kamchatka Peninsula is particularly suitable for investigating coseismic gravity changes across both land and ocean, including the effects of seawater redistribution. I estimated the coseismic gravity changes from GRACE Follow-On (GRACE-FO) observations and compared them with predictions from eight published finite-fault models without adjusting their source parameters. The observed gravity field exhibits a positive maximum of +3.2 μGal and a negative minimum of −4.3 μGal. Spatial correlations between the observed and predicted gravity changes vary substantially among the models. The Liu and Tang models show the highest correlations of 0.93 and 0.91, respectively, followed by the Yagi model (0.89). Correlations increase in regions exhibiting larger gravity changes, reaching approximately 0.98 for the Liu and Tang models at a threshold of 2.0 μGal. Comparisons of the amplitudes and locations of positive and negative gravity extrema further reveal differences among the predicted gravity fields. These results demonstrate that satellite gravity observations serve as an effective independent dataset capable of evaluating and constraining earthquake source models derived from conventional seismic, geodetic, and

tsunami data, even at the current observational resolution limits.

Keywords

2025 Kamchatka earthquake; GRACE Follow-On; Satellite gravimetry; Coseismic gravity changes; Finite-fault models; Earthquake source model validation

1. Introduction

On 29 July 2025, a great earthquake (Mw 8.8) occurred off the eastern coast of the Kamchatka Peninsula, Russia, along the Kuril–Kamchatka subduction zone, where the Pacific Plate subducts beneath the overriding plate. The earthquake ruptured a substantial portion of the plate interface and generated a trans-Pacific tsunami. The event occurred near the source region of the 1952 Kamchatka great earthquake (Mw ~9), providing an important opportunity to investigate the rupture characteristics of great earthquakes along this subduction zone. Following the 2025 event, numerous finite-fault models were proposed using different observational datasets, including seismic waveforms, Global Navigation Satellite System (GNSS) measurements, interferometric synthetic aperture radar (InSAR), and tsunami observations. Although these models describe the same megathrust earthquake, they differ in the spatial distribution, magnitude, and extent of coseismic slip (e.g., Liu et al., 2026; Himematsu and Munekane, 2026; Tang et al., 2026). Satellite gravimetry provides an independent means of investigating earthquakes by observing gravity changes associated with crustal deformation and mass redistribution.

The Gravity Recovery and Climate Experiment (GRACE) detected coseismic gravity changes associated with great subduction-zone earthquakes, including the 2004 Sumatra–Andaman, 2010 Maule, and 2011 Tohoku–Oki earthquakes (Han et al., 2006;

Heki and Matsuo, 2010; Matsuo and Heki, 2011). Its applicability was subsequently extended to deep-focus earthquakes, including the 2013 Okhotsk (Mw 8.3) and 2018 Fiji (Mw 8.2) events (Tanaka et al., 2015; Tanaka, 2023). GRACE and its successor, GRACE Follow-On (GRACE-FO), thus provide a means of examining coseismic deformation through regional gravity changes, complementing conventional seismic and geodetic observations.

A particularly important feature of satellite gravimetry is its sensitivity to mass redistribution associated with both land deformation and seawater displacement. Heki and Matsuo (2010) demonstrated that accounting for seawater substantially modifies the predicted coseismic gravity changes of the 2010 Maule earthquake, compared with calculations assuming a dry Earth. Tanaka (2023) further demonstrated the importance of seawater redistribution in the coseismic gravity changes of the 2018 Fiji deep-focus earthquake. Such effects may be especially important for the 2025 Kamchatka earthquake because the land–ocean distribution changes markedly along the strike of the megathrust owing to the peninsula's geometry. Consequently, even modest differences in the location and extent of fault slip may produce appreciable differences in the predicted gravity field through changes in the spatial distribution of crustal deformation and associated seawater displacement. Furthermore, conventional geodetic observations, such as GNSS and

InSAR, are often concentrated on land, whereas tsunami observations are obtained in the ocean. In contrast, GRACE/GRACE-FO observes regional gravity fields over both land and ocean, without being restricted by the geographical distribution of ground-based observation stations or land surfaces accessible to InSAR. This capability offers a geographically complementary perspective for independently evaluating finite-fault models derived from different observational datasets.

Despite the availability of numerous finite-fault models for the 2025 Kamchatka earthquake, a systematic evaluation of their predicted coseismic gravity changes using independent GRACE/GRACE-FO observations remains lacking. In this study, I estimate coseismic gravity changes from GRACE/GRACE-FO observations and calculate the corresponding gravity changes predicted by eight published finite-fault models using the formulation of Sun et al. (2009). Without adjusting the published source parameters, I quantitatively compare the predicted and observed gravity fields using spatial correlation coefficients, including comparisons restricted to regions with relatively large gravity changes, as well as the amplitudes and locations of positive and negative gravity anomalies. These comparisons allow us to assess the consistency of existing source models with satellite gravity observations and examine the ability and limitations of current satellite gravimetry to distinguish among alternative rupture models. The results

also provide a basis for evaluating the potential scientific contributions of future gravity satellite missions with improved observational capabilities.

2. Data and Forward Modeling

2.1. Satellite Gravity Data and Finite-Fault Models

In this study, unfiltered monthly Level-2 spherical harmonic solutions from the Center for Space Research (CSR), Release 6.3 (RL06.3), for the GRACE-FO missions are used. The data were obtained through the International Centre for Global Earth Models (ICGEM) and NASA Earthdata. The Stokes coefficients were used up to degree and order 60. Following the GRACE/GRACE-FO Technical Notes, the degree-2 and degree-3 zonal coefficients, (C_{20} and C_{30}), were replaced with estimates derived from satellite laser ranging (SLR), where recommended.

The temporal variations in the Stokes coefficients were converted into radial gravity disturbances following Wahr et al. (1998). To suppress short-wavelength noise, I applied a fan filter with a characteristic spatial scale of 250 km (Zhang et al., 2009). The resulting gravity disturbances, defined as positive downward, were evaluated on a 1° × 1° grid covering 145°–170°E and 40°–60°N. I used monthly observations from January 2020 through August 2026 for the temporal analysis described in Section 3.

For comparison with the satellite observations, I selected eight published finite-fault models of the 2025 Kamchatka earthquake, developed using different observational datasets and inversion methods.

The USGS NEIC preferred model (version 5) was obtained by joint kinematic inversion of teleseismic waveforms, Sentinel-1 InSAR, and GNSS observations, using three fault planes approximating the curved plate interface. Liu et al. (2026) combined teleseismic body and surface waves with Sentinel-1 InSAR in a kinematic inversion estimating slip, rake, rise time, and rupture velocity. Himematsu and Munekane (2026) estimated static slip from ALOS-2/PALSAR-2 InSAR observations using elastic dislocation models and spatial smoothing. Xiao et al. (2026) combined GNSS and Sentinel-1 InSAR observations in a constrained static inversion using a layered elastic Earth model. Fujii and Satake (2026) estimated fault slip by tsunami waveform inversion; I adopted their solution based exclusively on DART bottom-pressure records. Ishijima and Watada (2026) inverted two-dimensional tsunami sea-surface height anomalies observed by SWOT/KaRIn using dispersive tsunami simulations. Yagi et al. (2025) applied Potency Density Tensor Inversion to teleseismic P waves, representing rupture as a continuous potency-density distribution. Tang et al. (2026) combined ALOS-2 and Sentinel-1 InSAR with GNSS displacements in a static inversion using quadrilateral fault

patches; I adopted their preferred Model C.

These models provide source estimates derived from seismic, geodetic, and tsunami observations, with different fault geometries and slip distributions. I retained their published source parameters without optimizing them against the GRACE/GRACE-FO observations.

2.2. Forward Modeling of Coseismic Gravity Changes

I calculated the coseismic gravity changes predicted by the eight published finite-fault models using the spherical Earth dislocation theory of Sun et al. (2009). The total gravity change was obtained by superposing the contributions from individual fault patches. Because the published models employ different representations of fault geometry and slip, their parameters were converted into a common rectangular-dislocation format. Details of these conversions are provided in the Supplementary Document S1.

To account for the effects of seawater redistribution associated with coseismic seafloor deformation, I first calculated gravity changes and vertical surface displacements on a spatial grid finer than the $1^\circ \times 1^\circ$ grid used for the GRACE/GRACE-FO observations. I then applied the seawater correction following Heki and Matsuo (2010), accounting for the reduced density contrast between crustal rocks and seawater in oceanic regions. The

corrected gravity changes were subsequently expanded into spherical harmonics up to degree and order 60, subjected to the same 250 km fan filter (Zhang et al., 2009) as the satellite observations, and transformed back into the spatial domain.

The resulting gravity fields were evaluated over 145°–170°E and 40°–60°N. For quantitative comparisons, the predicted values were extracted at the same 1° × 1° grid points as the GRACE/GRACE-FO observations, without spatial interpolation. No additional amplitude scaling, spatial shifts, or constant offsets were applied to the calculated gravity changes.

Hereafter, each finite-fault model is referred to by the surname of the first author of the corresponding study, except for the USGS model.

3. Temporal Analysis and Observed Coseismic Gravity Changes

To estimate the coseismic gravity changes associated with the 2025 Kamchatka earthquake, I fitted the GRACE/GRACE-FO gravity time series at each grid point using the following function:

$$g(t) = a_0 + a_1 t + season(t) + earthquake(t) \quad (1)$$

$$season(t) = a_2 \sin(2\pi t) + a_3 \cos(2\pi t) + a_4 \sin(4\pi t) + a_5 \cos(4\pi t) \quad (2)$$

$$earthquake(t) = H(\Delta t)\left[C + P\left(1 - e^{-\frac{\Delta t}{\tau}}\right)\right] \quad (3)$$

where t is time in decimal years, $\Delta t = t - (2025 + 7/12)$ represents the elapsed time for the monthly observations, and H is the Heaviside step function. The coefficients a_0 to a_5, C and P represent the constants estimated by the least squares. C and P represent the coseismic gravity jump and the amplitude of postseismic gravity change, respectively, and τ is the time constant showing the characteristic timescale of the postseismic gravity change.

I assumed a common time constant for all 546 grid points and determined its value by minimizing the total sum of squared residuals over the study region. This yielded 0.847 yr. With this value fixed, the remaining coefficients were estimated independently at each grid point by linear least squares. Figure 1a shows the resulting spatial distribution of coseismic gravity changes. The gravity field exhibits a broad negative anomaly northwest of the rupture region and a positive anomaly to the southeast. The maximum positive gravity change is +3.21 μGal at 159°E, 49°N, whereas the minimum is −4.27 μGal at 153°E, 53°N.

Figure 1b shows the gravity time series at these two locations after removing the estimated linear trends and seasonal variations. The single-exponential model generally

178 reproduces the observed temporal variations, although deviations are apparent during the
179 early postseismic period.

180 As demonstrated by Tanaka and Heki (2014), postseismic gravity changes may
181 contain components with different characteristic timescales. I therefore also examined a
182 two-exponential model, adopting fixed time constants of 0.2 and 2.0 yr, to evaluate the
183 sensitivity of the coseismic estimates to the assumed temporal behavior. Notably, at the
184 negative coseismic peak (153°E, 53°N), the two-exponential fit exhibits an initial
185 postseismic decrease followed by a longer-term increase in gravity, consistent with the
186 contrasting short- and long-term postseismic behavior discussed by Tanaka and Heki
187 (2014). The corresponding fitted curves for the post-earthquake period are shown as
188 dashed lines in Figure 1b.

189 Although both temporal models provide broadly comparable fits to the
190 observations, their estimates of the coseismic gravity change differ. Comparison of the
191 resulting gravity maps indicates a temporal-model-dependent ambiguity of
192 approximately 1 μGal, in addition to observational uncertainties, reflecting the difficulty
193 of separating coseismic and early postseismic signals using monthly satellite gravity
194 observations. Nevertheless, the main conclusions of the finite-fault model comparisons
195 remain robust to the choice of temporal model, as demonstrated by the results obtained

196 using the two-exponential model in the Supplementary Document S2.

197

198 **4. Comparison with Published Finite-Fault Models**

199 Figures 2 and 3 show the coseismic gravity changes predicted by the eight
200 published finite-fault models, calculated using the procedure described in Section 2. All
201 predictions are displayed using the same color scale and contour interval as the observed
202 gravity changes in Figure 1a, allowing direct comparison of their spatial patterns and
203 amplitudes. Despite differences in the underlying fault models, all eight predictions
204 exhibit a broadly similar pattern, characterized by negative gravity changes northwest of
205 the rupture area and positive changes southeast of it. However, substantial differences are
206 evident in the amplitudes and spatial locations of these anomalies. For presentation, the
207 models are divided into two groups according to their spatial correlations with the
208 observations: Figure 2 shows Fujii, Ishijima, USGS, and Xiao, while Figure 3 shows
209 Himematsu, Liu, Tang, and Yagi.

210 To quantitatively evaluate the agreement in spatial patterns, I calculated Pearson
211 correlation coefficients between the observed and predicted gravity changes at the 546
212 common grid points (Table 1). The Liu and Tang models show the highest correlations,
213 with coefficients of 0.929 and 0.910, respectively, followed by the Yagi model (0.892).

The Himematsu and Fujii models yield correlations of 0.800 and 0.795, while the remaining models exhibit lower correlations ranging from 0.713 to 0.763. I also calculated correlations for subsets of grid points where the absolute gravity change in either the observations or predictions is at least 1.0, 1.5, or 2.0 μGal (Table 1). The correlations generally increase with increasing threshold. For example, at the 2.0 μGal threshold, the Liu, Tang, and Yagi models yield correlations of 0.984, 0.983, and 0.972, respectively. These threshold-dependent correlations describe the agreement in regions exhibiting relatively large gravity changes, although the selected grid points differ among models.

Table 1. Spatial correlations between observed and predicted coseismic gravity changes at different amplitude thresholds

Model	All grids	≥ 1.0 μGal	≥ 1.5 μGal	≥ 2.0 μGal
Fujii	0.795 (546)	0.823 (241)	0.872 (126)	0.922 (72)
Ishijima	0.745 (546)	0.764 (253)	0.805 (132)	0.908 (83)
USGS	0.763 (546)	0.786 (254)	0.833 (143)	0.858 (90)
Xiao	0.713 (546)	0.739 (303)	0.774 (187)	0.812 (120)
Himematsu	0.800 (546)	0.841 (241)	0.884 (129)	0.946 (77)
Liu	0.929 (546)	0.947 (234)	0.971 (123)	0.984 (71)
Tang	0.910 (546)	0.931 (239)	0.958 (123)	0.983 (77)
Yagi	0.892 (546)	0.914 (246)	0.948 (141)	0.972 (89)

Pearson correlation coefficients between observed and predicted gravity changes. Values in parentheses indicate the number of grid points used. For each threshold, grid points were selected where the absolute gravity change in either the observations or predictions was equal to or greater than the specified threshold.

241 Table 2. Comparison of positive and negative gravity extrema between observations and

242 finite-fault models

	Positive peak				Negative peak			
Model	Amp.	Loc.(E N)	ΔAmp.	Dist.	Amp.	Loc.(E N)	ΔAmp.	Dist.
Obs.	+3.2	159 49			-4.3	153 53		
Fujii	+2.0	159 49	-1.2	0	-2.8	155 53	+1.4	134
Ishijima	+5.4	159 50	+2.2	111	-3.0	154 54	+1.3	129
USGS	+3.2	161 49	0.0	146	-6.2	155 52	-1.9	175
Xiao	+6.3	156 49	+3.1	219	-6.2	153 54	-1.9	111
Himematsu	+4.1	161 50	+0.9	182	-2.9	155 53	+1.4	134
Liu	+3.1	160 50	-0.1	133	-4.0	154 53	+0.3	67
Tang	+3.8	160 50	+0.6	133	-3.4	153 53	+0.8	0
Yagi	+5.1	161 50	+1.9	182	-6.6	154 52	-2.3	130

243 Amplitudes and locations of the positive and negative extrema of observed and predicted

244 coseismic gravity changes. ΔAmp. represents the predicted minus observed peak

245 amplitude, calculated before rounding. Distance indicates the great-circle distance

246 between the predicted and observed peak locations.

247

Table 2 compares the amplitudes and locations of the positive and negative gravity extrema. The observations yield a positive maximum of +3.21 μGal at 159°E, 49°N and a negative minimum of −4.27 μGal at 153°E, 53°N. The Liu model predicts extrema of +3.08 and −3.95 μGal, closely reproducing the observed amplitudes, while the Tang model predicts +3.80 and −3.43 μGal and reproduces the location of the negative extremum. In contrast, the Fujii model underestimates the amplitudes of both extrema, whereas the Xiao and Yagi models substantially overestimate them. The USGS model reproduces the positive amplitude relatively well but overestimates the magnitude of the negative anomaly. Differences in the locations of the extrema are also apparent among the models, providing an additional measure of agreement beyond the spatial correlation coefficients.

Taken together, the spatial correlations and comparisons of the gravity extrema reveal appreciable differences in the agreement between the published finite-fault models and the independently observed satellite gravity changes. The Liu and Tang models show particularly good agreement in both spatial patterns and extrema, although the relative performance of the models depends on the aspect of the gravity field being evaluated.

5. Discussion

The comparison of eight published finite-fault models demonstrates the potential of GRACE/GRACE-FO observations to provide independent constraints on earthquake source models. Several models reproduce the observed coseismic gravity pattern without any adjustment of their source parameters, with spatial correlation coefficients exceeding 0.9. Unlike GNSS and InSAR observations, which are primarily available over land, satellite gravimetry provides gravity observations across both continental and oceanic regions. This characteristic is particularly relevant to the 2025 Kamchatka earthquake, for which the rupture extends along a peninsula separating continental and oceanic environments. Furthermore, the contribution of seawater redistribution to the gravity field makes satellite gravimetry sensitive to aspects of seafloor deformation that may not be fully constrained by land-based geodetic observations. The observed gravity changes therefore provide a complementary test of finite-fault models developed using seismic, geodetic, and tsunami observations.

Although the Liu and Tang models show particularly high agreement with the observations, identifying a uniquely preferred source model remains difficult. Spatial correlations mainly characterize the agreement in geographical patterns and do not directly measure the agreement in absolute amplitudes. Conversely, comparisons of

284 positive and negative gravity extrema emphasize localized features rather than the entire
285 gravity field. To summarize these complementary measures, I performed an exploratory
286 principal component analysis using five standardized variables: the spatial correlation
287 coefficient and the absolute amplitude and location differences of the positive and
288 negative extrema. The first principal component explains 51.8% of the total variance,
289 with the Liu and Tang models obtaining the highest scores. However, small differences
290 in the agreement between source models should not be interpreted as definitive evidence
291 favoring one model over another because the ability to distinguish among competing
292 finite-fault models is limited by the spatial and temporal resolution of current
293 GRACE/GRACE-FO observations. Their limited spatial resolution obscures differences
294 in the finer-scale gravity signatures predicted by individual models, while their monthly
295 temporal resolution makes it difficult to separate instantaneous coseismic gravity changes
296 from deformation occurring during the earliest postseismic period. The sensitivity
297 analysis in Supplementary Document S2 indicates that the choice of temporal model
298 introduces differences of approximately 1 μGal in the estimated coseismic gravity
299 changes.

300 Future satellite gravimetry missions with improved spatial resolution, temporal
301 sampling, and measurement precision could strengthen the ability to discriminate among

competing earthquake source models. In particular, the differences in predicted gravity fields among independently developed finite-fault models provide a useful basis for evaluating the observational performance required of future missions. Such evaluations are among the objectives of FEATS-G (Quantifying the Potential of Quantum Space Gravimetry), an international research project investigating the potential benefits of quantum-sensor-based satellite gravimetry through numerical mission simulations (GFZ German Research Centre for Geosciences 2026).

Most importantly, the present findings demonstrate that satellite gravimetry already provides an effective and independent benchmark for evaluating earthquake source models derived from conventional observations. The results also establish an empirical foundation for assessing the observational performance required of next-generation satellite gravimetry missions.

Abbreviations

CSR: Center for Space Research

GNSS: Global Navigation Satellite System

GRACE: Gravity Recovery And Climate Experiment

GRACE-FO: Gravity Recovery And Climate Experiment Follow-On

ICGEM: International Centre for Global Earth Models

InSAR: Interferometric Synthetic Aperture Radar

NEIC: National Earthquake Information Center

PCA: Principal Component Analysis

SLR: Satellite Laser Ranging

USGS: United States Geological Survey

Declarations

Ethics approval and consent to participate

Not applicable.

Consent for publication

Not applicable.

Availability of data and materials

The GRACE-FO Level-2 spherical harmonic coefficients used in this study are publicly available through the International Centre for Global Earth Models (ICGEM; https://icgem.gfz.de/) and NASA Earthdata (https://www.earthdata.nasa.gov/; https://doi.org/10.5067/GFL20-MC063). The satellite laser ranging (SLR) estimates used to replace the C20 and C30 coefficients are provided in GRACE Technical Note 14,

available through the NASA Earthdata GRACE/GRACE-FO documentation (https://www.earthdata.nasa.gov/data/platforms/space-based-platforms/grace-grace-fo/documentation). The published finite-fault models are available from the original sources cited in this study, including the USGS National Earthquake Information Center. The analysis procedures are described in the main text, with details of the finite-fault parameter conversions provided in the Supporting Information. The derived results supporting the model comparisons are presented in the tables and figures of this article and its Supporting Information.

Competing interests

The author declares that there are no competing interests.

Funding

This research received no external funding.

Authors' contributions

The author performed the research, analyzed the data, and wrote and approved the manuscript.

Acknowledgements

The figures in this study were prepared using the Generic Mapping Tools (GMT) version 6 (Wessel et al. 2019).

References

Fujii Y, Satake K (2026) The slip distributions of the 1952 and 2025 Kamchatka earthquakes from tsunami waveforms recorded around the Pacific Ocean. Geophys Res Lett **53**. https://doi.org/10.1029/2025GL120682

GFZ German Research Centre for Geosciences (2026) FEATS-G: Quantifying the potential of quantum space gravimetry. https://www.gfz.de/en/section/earth-system-modelling/projects/feats-g-quantifying-the-potential-of-quantum-space-gravimetry. Accessed 6 Nov 2026

GRACE-FO (2024) GRACE-FO Level-2 monthly geopotential spherical harmonics CSR Release 06.3. Version 6.3. NASA Physical Oceanography Distributed Active Archive Center (PO.DAAC). https://doi.org/10.5067/GFL20-MC063

Han SC, Shum CK, Bevis M, Ji C, Kuo CY (2006) Crustal dilatation observed by GRACE after the 2004 Sumatra-Andaman earthquake. Science **313**: 658–662. https://doi.org/10.1126/science.1128661

Heki K, Matsuo K (2010) Coseismic gravity changes of the 2010 earthquake in central Chile from satellite gravimetry. Geophys Res Lett **37**. https://doi.org/10.1029/2010GL045335

374 Himematsu Y, Munekane H (2026) Shallow segment rupture associated with the 2025
375 Kamchatka earthquake inferred from ALOS-2/PALSAR-2 InSAR. Earth Planets
376 Space **78**: 66. https://doi.org/10.1186/s40623-026-02437-4
377 Ishijima K, Watada S (2026) The slip distribution of the 2025 Kamchatka earthquake
378 determined from SWOT satellite dispersive tsunami images. Earth Planets Space **78**:
379 176. https://doi.org/10.1186/s40623-026-02508-6
380 Liu C, Bai Y, Lay T, He P, Wen Y, Xiong X, Taymaz T (2026) Simple unilateral rupture
381 of the great Mw 8.8 2025 Kamchatka earthquake. Science **391**: 812–817.
382 https://doi.org/10.1126/science.aeb8232
383 Matsuo K, Heki K (2011) Coseismic gravity changes of the 2011 Tohoku-Oki earthquake
384 from satellite gravimetry. Geophys Res Lett **38**.
385 https://doi.org/10.1029/2011GL049018
386 Sun W, Okubo S, Fu G, Araya A (2009) General formulations of global co-seismic
387 deformations caused by an arbitrary dislocation in a spherically symmetric earth
388 model—applicable to deformed earth surface and space-fixed point. Geophys J Int
389 **177**: 817–833. https://doi.org/10.1111/j.1365-246X.2009.04113.x
390 Tanaka Y (2023) Coseismic gravity changes and crustal deformation induced by the 2018
391 Fiji deep-focus earthquake observed by GRACE and GRACE-FO satellites. Remote

Sens **15**: 495. https://doi.org/10.3390/rs15020495

Tanaka Y, Heki K (2014) Long- and short-term postseismic gravity changes of megathrust earthquakes from satellite gravimetry. Geophys Res Lett **41**: 5451–5456. https://doi.org/10.1002/2014GL060559

Tanaka Y, Heki K, Matsuo K, Shestakov NV (2015) Crustal subsidence observed by GRACE after the 2013 Okhotsk deep-focus earthquake. Geophys Res Lett **42**: 3204–3209. https://doi.org/10.1002/2015GL063838

Tang CH, Fukushima Y, Okada Y, Mizutani A (2026) Lateral extent of coseismic slip and limited shallow rupture during the 29 July 2025 Kamchatka earthquake illuminated by geodetic and tsunami data. Geosci Lett **13**: 21. https://doi.org/10.1186/s40562-026-00471-4

US Geological Survey (2025) M 8.8 – 2025 Kamchatka Peninsula, Russia earthquake. USGS Earthquake Hazards Program. https://earthquake.usgs.gov/earthquakes/eventpage/pt25210002/. Accessed 6 Nov 2026

Wahr J, Molenaar M, Bryan F (1998) Time variability of the Earth's gravity field: Hydrological and oceanic effects and their possible detection using GRACE. J Geophys Res **103**: 30205–30229. https://doi.org/10.1029/98JB02844

Wessel P, Luis JF, Uieda L, Scharroo R, Wobbe F, Smith WHF, Tian D (2019) The Generic Mapping Tools version 6. Geochem Geophys Geosyst **20**: 5556–5564. https://doi.org/10.1029/2019GC008515

Xiao Y, Wang J, Zhang Y, Zhang W, Zhou J, Sun H, Zhao Y, Osman A, Guo R (2026) Interseismic, coseismic, and early postseismic slip associated with the 2025 Mw 8.8 Kamchatka earthquake. Geophys Res Lett **53**. https://doi.org/10.1029/2025GL121473

Yagi Y, Fukahata Y, Okuwaki R, Takagawa T, Toda S (2025) Breaking the cycle: Short recurrence and overshoot of an M9-class Kamchatka earthquake. Seismica **4** (2). https://doi.org/10.26443/seismica.v4i2.2012

Zhang ZZ, Chao BF, Lu Y, Hsu HT (2009) An effective filtering for GRACE time-variable gravity: Fan filter. Geophys Res Lett **36**. https://doi.org/10.1029/2009GL039459

Figure legends

Figure 1. Observed coseismic gravity changes associated with the 2025 Kamchatka earthquake. (a) Spatial distribution of the coseismic gravity change estimated from GRACE/GRACE-FO observations using the single-exponential (1-exp) temporal model. The contour interval is 0.5 μGal. The red rectangle schematically indicates the fault area, and the beach ball represents the focal mechanism plotted at the epicenter. (b) Gravity time series at 159°E, 49°N (red) and 153°E, 53°N (blue), corresponding to the positive (+3.21 μGal) and negative (−4.27 μGal) extrema in (a), respectively. The temporal analysis uses data from January 2020 onward, whereas only data from January 2024 onward are displayed. Black circles represent the observed gravity changes after removal of the fitted background components (linear trend, annual and semiannual variations). Solid and dashed curves represent the fitted 1-exp and two-exponential (2-exp) temporal models, respectively. The 2-exp curves are shown only after the earthquake. Error bars indicate ±1 standard deviation of the residuals from the 1-exp fit at each location, rather than formal measurement uncertainties. The upper time series is vertically offset for clarity.

Figure 2. Predicted gravity changes from the Fujii, Ishijima, USGS, and Xiao models. (a) Fujii, (b) Ishijima, (c) USGS, and (d) Xiao models. The spatial resolution and color scale are identical to those in Figure 1a, with a contour interval of 0.5 μGal. The red rectangle schematically indicates the fault area, and the beach ball represents the focal mechanism plotted at the epicenter.

Figure 3. Predicted gravity changes from the Himematsu, Liu, Tang, and Yagi models. (a) Himematsu, (b) Liu, (c) Tang, and (d) Yagi models. The spatial resolution, color scale, and contour interval are identical to those in Figure 2. The red rectangle schematically indicates the fault area, and the beach ball represents the focal mechanism plotted at the epicenter.

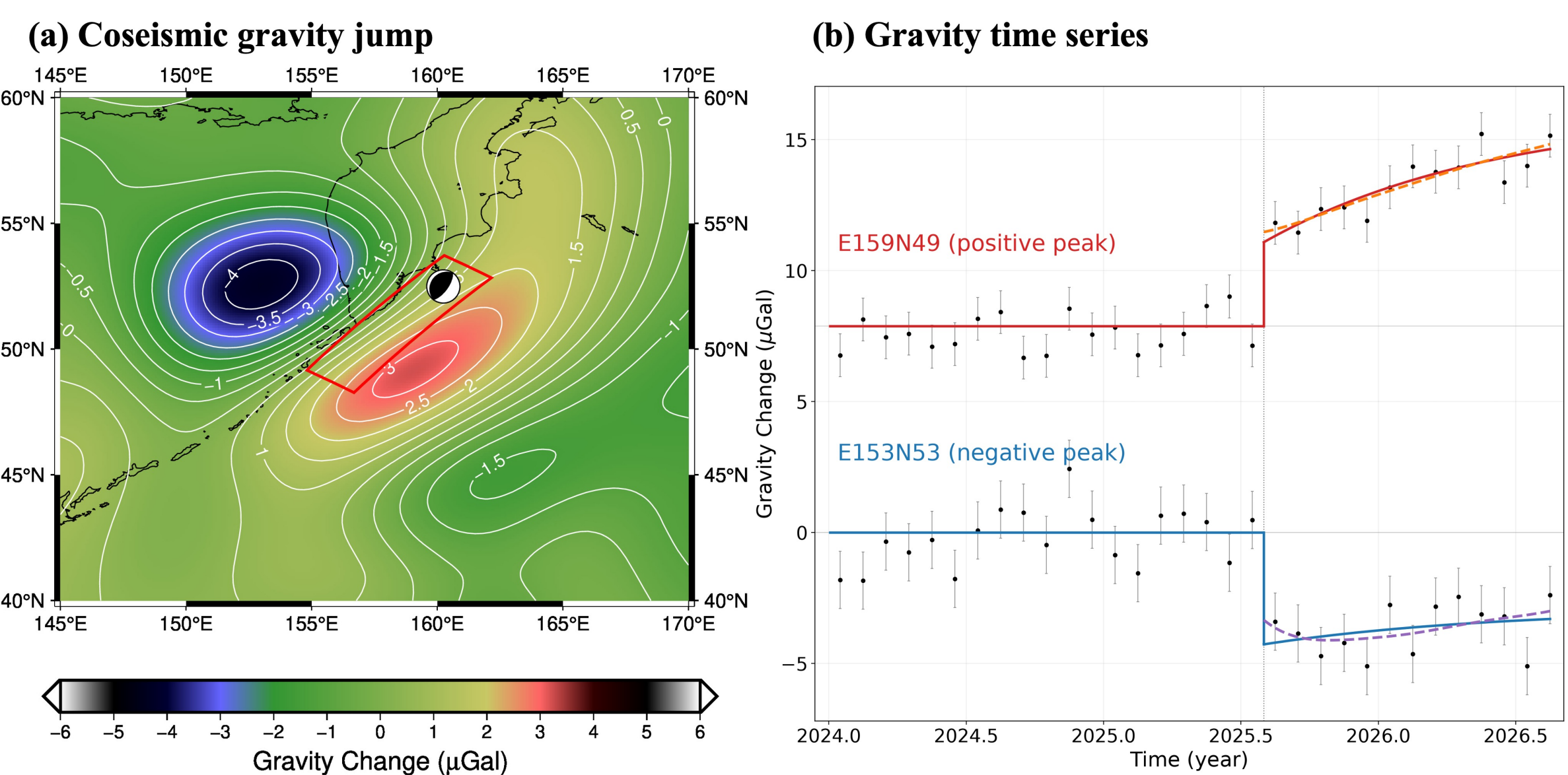
(a) Coseismic gravity jump
145°E
150°E
155°E
160°E
165°E
170°E
60°N
55°N
50°N
45°N
40°N
−6
−5
−4
−3
−2
−1
0
1
2
3
4
5
6
Gravity Change (μGal)
(b) Gravity time series
E159N49 (positive peak)
E153N53 (negative peak)
Gravity Change (μGal)
Time (year)
2024.0
2024.5
2025.0
2025.5
2026.0
2026.5

(a) Fujii model

(b) Ishijima model

(c) USGS model

(d) Xiao model

145°E 150°E 155°E 160°E 165°E 170°E

60°N 55°N 50°N 45°N 40°N

Gravity Change (μGal)

6 5 4 3 2 1 0 −1 −2 −3 −4 −5 −6

(a) Himematsu model

(b) Liu model

(c) Tang model

(d) Yagi model

145°E 150°E 155°E 160°E 165°E 170°E

60°N 55°N 50°N 45°N 40°N

Gravity Change (μGal)

6 5 4 3 2 1 0 −1 −2 −3 −4 −5 −6

Supplementary Files

This is a list of supplementary files associated with this preprint. Click to download.

- SupplementaryDocumentS1.pdf
- SupplementaryDocumentS2.docx
- SupportingInformation.docx
- graphicalabstract920x300.png